Strain generated by the stacking faults in epitaxial SrO(SrTiO 3) N Ruddlesden–Popper structures

Guillaume Saint-Girons, Clarisse Furgeaud, Ludovic Largeau, Alexandre Danescu, Romain Bachelet, Mohamed Bouras

electronic reprint

JOURNAL OF APPLIED CRYSTALLOGRAPHY

ISSN: 1600-5767
journals.iucr.org/j

Strain generated by the stacking faults in epitaxial $SrO(SrTiO_3)_N$ Ruddlesden–Popper structures

Guillaume Saint-Girons, Clarisse Furgeaud, Ludovic Largeau, Alexandre Danescu, Romain Bachelet and Mohamed Bouras

J. Appl. Cryst. (2023). **56**, 1426–1434

JOURNAL OF APPLIED CRYSTALLOGRAPHY

ISSN 1600-5767

Received 14 June 2023
Accepted 6 August 2023

Edited by J. Keckes, Montanuniversität Leoben, Austria

Keywords: Ruddlesden–Popper compounds; defects; X-ray diffraction.

Supporting information: this article has supporting information at journals.iucr.org/j

Strain generated by the stacking faults in epitaxial $SrO(SrTiO_3)_N$ Ruddlesden–Popper structures

Guillaume Saint-Girons,[a]* Clarisse Furgeaud,[a] Ludovic Largeau,[b] Alexandre Danescu,[a] Romain Bachelet[a] and Mohamed Bouras[a,c]

[a]INL-UMR5270/CNRS-Ecole Centrale de Lyon, French National Centre for Scientific Research, 36 avenue Guy de Collongue, Lyon, Ecully 69134, France, [b]C2N/CNRS, Université Paris-Saclay, Palaiseau, 91120, France, and [c]GEMAC, CNRS/UVSQ, 45 avenue des Etats Unis, Bat. Fermat, Versailles, 78035, France. *Correspondence e-mail: guillaume.saint-girons@ec-lyon.fr

Ruddlesden–Popper (RP) phases present outstanding physical properties triggering significant academic interest. Out-of-plane stacking faults (OP-SFs), which are the main channel for accommodating stoichiometry imbalance in RP thin layers, affect these properties. The mechanisms underlying the formation and spatial distribution of these defects remain largely unknown to date. This work shows that the residual mismatch related to the presence of OP-SFs in $SrTiO_3$-based RP thin layers is accommodated by a delocalized mechanism of lateral strain transfer from the disturbed regions to the RP structure, generating a distribution of compressive strain in the latter. Analysing the RP X-ray diffractograms in the light of this mechanism allows the assessment of the OP-SF distribution along the growth axis. It also allows the separate and accurate determination of the $SrTiO_3$ lattice parameter (c = 3.9214 ± 0.0003 Å) and the SrO–SrO inter-reticular distance (d = 2.549 ± 0.001 Å) in the RP structure.

1. Introduction

An Nth-order $SrTiO_3$ (STO) Ruddlesden–Popper phase (RP[N]), of chemical formula $(SrO)(SrTiO_3)_N$, consists of an STO perovskite structure in which one extra SrO plane is inserted every N STO unit cells along the (00l) direction (Ruddlesden & Popper, 1957, 1958). This extra plane forms a stacking fault (SF). The RP phases trigger significant academic interest due to their outstanding functional properties. Among others, RP phases based on STO or other perovskite oxides ($SrRuO_3$, $LaCuO_3$, $NdNiO_3$ *etc.*) exhibit very low dielectric losses (Dawley *et al.*, 2020*b*; McCarthy *et al.*, 1969; Lee *et al.*, 2013*b*), strong magnetoresistance (Moritomo *et al.*, 1996), improper ferroelectricity (Birol *et al.*, 2011; Pitcher *et al.*, 2015; Oh *et al.*, 2015; Benedek *et al.*, 2015) or low thermal conductivity, with attractive prospects for the design of high-efficiency thermoelectric modules (Balachandran *et al.*, 2017; Dawley *et al.*, 2021; Wise *et al.*, 2001; Kamba *et al.*, 2003).

As expected, RP[N] electronic properties depend on N (Lee *et al.*, 2006, 2013*b*), enabling flexibility for functional design. However, RP phase fabrication is a challenging task, as one has to control the growth process at the monolayer level. Hence, modelling shows that all RP[N] with $N > 2$ (or $N > 3$, depending on the authors) have comparable formation enthalpies, leading to a strong phase-mixing tendency (Yang *et al.*, 2022; Noguera, 2000; McCoy *et al.*, 1997; Udayakumar & Cormack, 1998). RP[N>3] synthesis from melt growth is therefore difficult or even impossible: it leads to defective RP mixtures or separation into STO and $N \leq 3$ phases (McCarthy *et al.*, 1969; Tilley, 1977; Liu *et al.*, 2016). Epitaxial growth

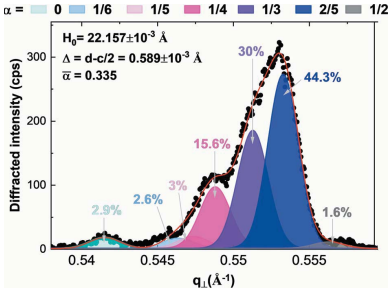

enables control of the stacking sequence, which makes RP phase fabrication considerably easier (Nie *et al.*, 2014; Lee *et al.*, 2014). Molecular-beam epitaxy (MBE), well adapted for such atomic layered growth, has previously been used to grow STO-based RP thin layers, with N up to 50 (Nie *et al.*, 2014; Lee *et al.*, 2014; Barone *et al.*, 2022; Haeni *et al.*, 2001; Jungbauer *et al.*, 2014; Haislmaier *et al.*, 2016; Barone *et al.*, 2021; Orloff *et al.*, 2009; Iwazaki *et al.*, 1999). Pulsed laser deposition has also been used to grow $N \leq 3$ STO-based RP layers (Okude *et al.*, 2008; Shibuya *et al.*, 2008). However, the higher the RP order, the more tightly the cationic composition must be controlled. Any composition imbalance is accommodated by disturbing the SF distribution, as predicted by calculation (McCoy *et al.*, 1997) and confirmed experimentally (Lee *et al.*, 2013*a*,*b*; Dawley *et al.*, 2020*a*,*b*; McCoy *et al.*, 1997; Nie *et al.*, 2014; Haeni *et al.*, 2001; Jungbauer *et al.*, 2014; Haislmaier *et al.*, 2016; Iwazaki *et al.*, 1999; Shibuya *et al.*, 2008; Tian *et al.*, 2001, 2007; Hawkins *et al.*, 1991; Williams *et al.*, 1991; Seshadri *et al.*, 1997; Sloan *et al.*, 1998; Zhu *et al.*, 2011).

In an ideal RP[N] grown on an (001)-oriented substrate, the SF distribution corresponds to exactly one infinite 'horizontal' SF plane (parallel to the substrate surface, denoted IP-SF in this article) every N STO unit cells. In an RP[N] grown under Sr/Ti stoichiometry imbalance conditions, parasitic 'vertical' SF planes [parallel to (0l0) and (l00), denoted OP-SFs hereinafter] of finite extent and parasitic interruption of the IP-SF occur, so that the global SF concentration accommodates this imbalance. This leads to a characteristic paved microstructure (Tian *et al.*, 2001; Jungbauer *et al.*, 2014) which can also be described as the presence of RP[$M \neq N$] intergrowths (IGs) locally disturbing the RP[N] matrix, separated from the latter by OP-SFs (Tian *et al.*, 2001). Fleck *et al.* (2022) reported a method based on transmission electron microscopy (TEM) phase image analysis to detect IGs accurately in RP samples. The lowest IG concentrations reported to date are 6% in an RP[4] matrix and 23% in an RP[5] matrix (Tian *et al.*, 2001). The highest-order RP reported to date is an RP[50] grown by MBE, with a 90 μm^{-1} OP-SF density (to be compared with the 51 μm^{-1} IP-SF density corresponding to RP[50] structuration) (Barone *et al.*, 2022).

The mechanisms underlying the generation and organization of SFs in RP layers are still poorly understood. The few literature reports dealing with this issue tend to emphasize the role of lateral lattice mismatch minimization (Tian *et al.*, 2001). Notably, Stone *et al.* (2016) showed that the strain generated by the OP-SFs in an RP[6] matrix is quite moderate (~2%) and is accommodated in the RP region rather than in the defective IG region. The study reported here decisively sheds new light on this problem.

2. Experimental

The two samples considered in this work were grown by solid-source MBE, using effusion cells to evaporate Sr and Ti. The growths were performed on as-received STO(001) substrates annealed at 700°C for 45 min under a molecular oxygen (O_2) partial pressure of 10^{-7} Torr. After annealing, for each of the two samples, TiO_2 was deposited under reflection high-energy electron diffraction (RHEED) monitoring, until the brightness of the half-order streak along the [100] RHEED azimuth was maximized, which corresponds to a TiO_2-terminated STO surface (Castell, 2002; Kajdos & Stemmer, 2014; Razaghi Pey Ghaleh *et al.*, 2021).

For the first (calibration) sample, STO was grown by co-depositing Sr and Ti at 700°C under a partial O_2 pressure of 10^{-7} Torr, and by tuning the Sr and Ti cell temperatures to suppress/minimize the half-order streaks on the RHEED patterns along the [100], [210] and [110] azimuths (Fig. S1 in the supporting information), which correspond to stoichiometric growth conditions for STO (Sr concentration = Ti concentration) within a 6–7% uncertainty (Razaghi Pey Ghaleh *et al.*, 2021). X-ray reflectivity and X-ray diffraction (XRD) measurements were then performed on the calibration sample (Fig. S1) to confirm the composition and to measure the sample thickness and growth rate. The latter was found to be 1.4 monolayers per minute (ML min^{-1}).

The second (RP[5]) sample was grown under the exact same conditions (growth temperature, growth rate, Sr and Ti cell temperatures, O_2 partial pressure) as the calibration sample by alternating SrO and TiO_2 ML deposition to form the RP[5] lattice. The growth sequence is sketched in Fig. S2: 20 RP half-periods were deposited on the STO substrate by reproducing the RP stacking sequence, starting from an IP-SF (two successive SrO planes). The stacking sequence for a single RP half-period thus reads (1 ML SrO) + 5[(1 ML SrO) + (1 ML TiO_2)]. Before growing the first RP half-period, an extra SrO ML was deposited on the TiO_2-terminated STO substrate as the first layer of the sequence to enhance the RP structural quality, taking advantage of the TiO_2/SrO swapping mechanism described by Nie *et al.* (2014) and Lee *et al.* (2014). This extra SrO ML remains on the growth front throughout the entire growth process (it acts as a surfactant) and promotes crystallization.

After growth, the RP[5] sample was characterized using XRD and TEM. For the XRD experiments, a Rikagu SmartLab diffractometer equipped with a high-brilliance (9 kW) rotating anode and a two-bounce monochromator on the incident beam was used. In this configuration, the θ (Bragg angle) resolution is ~0.008°. High-angle annular dark-field scanning transmission electron microscopy (HAADF-STEM) cross-sectional views of the sample were also recorded. The images displayed in Figs. 1 and Fig. 4(*b*) were recorded using a ThermoFisher Titan Themis 200 FEI equipped with a probe aberration corrector allowing atomically and chemically resolved images, while that shown in Fig. 4(*a*) was recorded using a JEOL JEM-ARM200F Cold FEG NeoARM 60–200 kV probe-corrected microscope, operated at 200 kV and equipped with a spherical aberration corrector (Cs probe CEOS ASCOR).

3. Results and discussion

The large-field HAADF-STEM cross-sectional image displayed in Fig. 1(*a*) gives an overview of the RP[5] sample

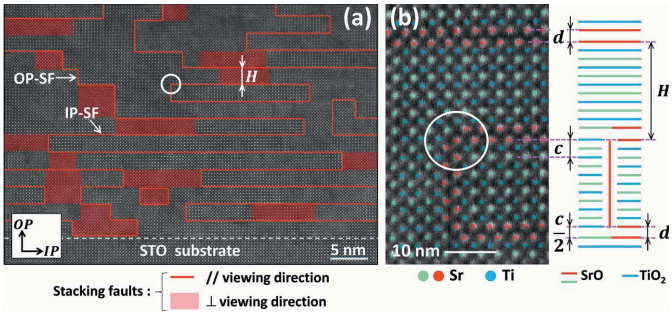

Figure 1
(*a*) A HAADF-STEM cross-sectional view of the RP[5] sample. Red lines highlight SFs lying parallel to the viewing direction, while red boxes indicate SFs lying perpendicular to the viewing direction, contained within the TEM foil thickness. OP and IP designate the out-of-plane ([00*l*], normal to the substrate surface) and the in-plane ([*l*00] and [0*l*0], contained in the substrate surface) directions, respectively. (*b*) A restrained field image emphasizing the atomic arrangement around OP-SFs and IP-SFs. Green dots/lines correspond to Sr atoms/SrO planes, blue dots/lines correspond to Ti atoms/TiO_2 planes and red dots/lines represent the Sr atoms/SrO planes forming the SF. *d* designates the distance between two subsequent SrO planes at an IP-SF, *c*/2 is the SrO–TiO_2 or TiO_2–SrO interplanar distance, and *H* is the RP half-period. In both panels, the white circles highlight the corner defects.

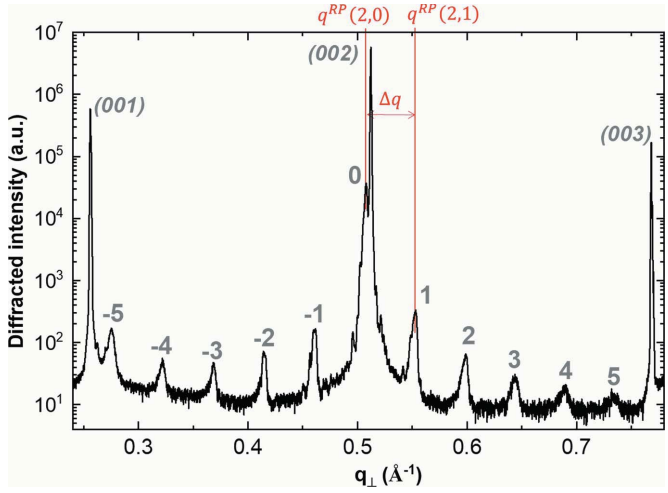

Figure 2
Large-scale out-of-plane radial XRD scan recorded on the RP[5] sample, showing RP diffraction orders from −5 to 5. Bracketed indices refer to STO substrate reflections.

microstructure. In this image and later in the paper, OP and IP designate the out-of-plane ([00*l*], normal to the substrate surface) and in-plane ([*l*00] and [0*l*0], contained in the substrate surface) directions, respectively.

This microstructure is typical for a defective RP layer: the RP[5] arrangement is disturbed by OP-SFs. OP-SFs lying parallel to the viewing direction, marked as red lines in Fig. 1(*a*), locally induce double SrO planes and an increased interplanar distance, which enables their detection in the image. OP-SFs lying perpendicular to the viewing direction and contained in the TEM foil thickness, marked as red boxes in Fig. 1(*a*), are more difficult to detect. However, they shift the structure by half a unit cell along the ⟨110⟩ directions, so that Sr and Ti atoms contribute simultaneously to the contrast in these regions. This homogenizes the atomic column contrast, while the contrast produced by the Sr columns is stronger than that produced by the Ti columns in defect-free regions, due to higher *Z* (Stone *et al.*, 2016; Tokuda *et al.*, 2011). Remarkably, each OP-SF endpoint is systematically associated with an IP-SF endpoint, and conversely each IP-SF endpoint is shared with an OP-SF endpoint, leading to the formation of 'corner defects' (circled in Fig. 1). Simple considerations provide a rough understanding for the formation of such defects: from both sides of a corner defect, the stacking sequence along OP changes from SrO–SrO (with an interplanar distance *d*) to SrO–TiO_2 or TiO_2–SrO (with a relaxed interplanar distance *c*/2); $d \simeq 2.6$ Å according to the literature (Ohnishi *et al.*, 2008; Venkateswaran *et al.*, 1987; Saint-Girons *et al.*, 2016), while *c*/2 is expected to be close to half the STO lattice parameter, that is 1.9525 Å. The local strain generated by a corner defect thus reads $(1/d)[(c/2) - d] \simeq -25$. It is much smaller in absolute terms than that generated by an IP-SF endpoint not associated with an OP-SF [namely, $(c - d)/d \simeq 50\%$], but remains very high and is thus unlikely to be accommodated locally, as confirmed by the results discussed below.

Fig. 2 shows a large-scale out-of-plane radial XRD scan recorded on the RP[5] sample. Despite crystal structure disturbances caused by the OP-SFs, the global shape of the curve is consistent with what is expected for an RP[5] lattice: it features a central zeroth-order peak near the STO (002) substrate reflection and ten satellite peaks (from −5 to 5) due to RP periodicity. To interpret this pattern, it is convenient to describe the RP[*N*] stack as a superlattice of period $H = d + 2Nc/2$ (superlattice period ⇔ RP half-period) including $2N + 1$ atomic planes (two successive SrO planes forming the IP-SFs and $2N - 1$ TiO_2–SrO planes; see the supporting information, Section S2). The average pseudo-cubic lattice parameter of the RP superlattice obeys $\overline{c}^{RP} = 2H/(2N + 1)$. In this description, the average and satellite peak positions are given by (Birch *et al.*, 1995; Bowen & Tanner, 1998)

$$q^{RP}(L, i) = \frac{L(2N+1)}{2H}\left[1 + \frac{2i}{L(2N+1)}\right] = \frac{L}{\overline{c}^{RP}}\left[1 + \frac{2i}{L(2N+1)}\right], \quad (1)$$

where *L* is the diffraction order (*L* = 2 in Fig. 2) and *i* is the satellite order (*i* = −5 to 5 in Fig. 2).

A closer look at the diffractogram of Fig. 2 allows us to capture its complexity (Fig. 3). The central and satellite peaks are broadened, displaying quite well resolved shoulders/components (marked by arrows). Neither the positions nor even less the intensities of these shoulders are compatible with thickness fringes, as discussed in the supporting information (Section S4). Each satellite peak exhibits similar structuration, suggesting that the latter is related to a modulation of the RP period. One may also note the presence of a series of reflections, marked by red stars in Fig. 3, decorating the right-hand side of the zeroth-order peak.

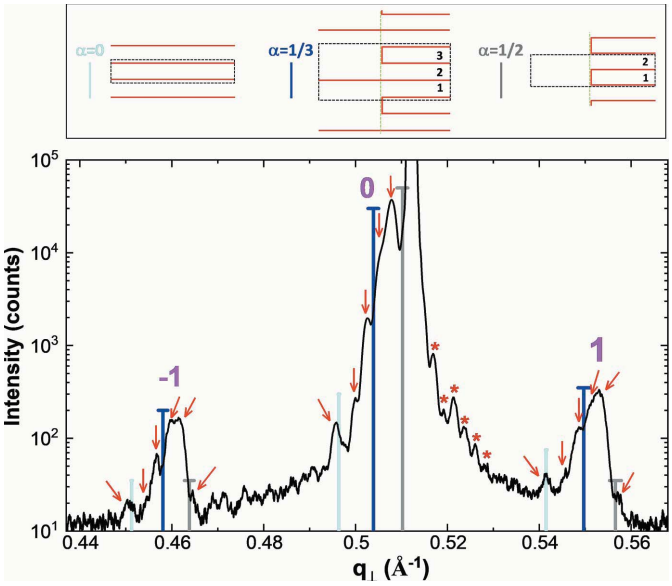

Figure 3
An enlargement of the central region of the diffractogram of Fig. 2. Red arrows indicate the shoulders resulting from RP half-period modulation due to OP-SFs and red stars indicate reflections corresponding to lattice strain modulation with a period corresponding to the vertical extension of the supercells. The bars indicate the expected positions for the reflections of RP_0 (light blue), $RP_{1/2}$ (grey) and $RP_{1/3}$ regions (dark blue), as deduced from TEM. For the RP_0 and $RP_{1/3}$ regions, these positions are directly extracted from the HAADF-STEM images of Figs. 4(*a*) and 4(*b*), respectively. For the $RP_{1/2}$ region, they are deduced from equation (1) and the value of H_0 extracted from the HAADF-STEM image of Fig. 4(*a*). The width of the bar caps represents the uncertainty on the reflection positions. The supercells corresponding to these three configurations are delimited by black dotted boxes in the top panel sketch.

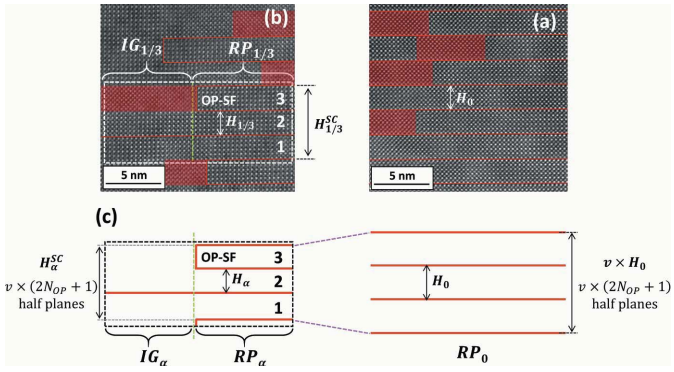

Figure 4
(*a*) A HAADF-STEM cross-sectional view of a zone of the RP[5] sample free of any OP-SFs parallel to the viewing direction and containing few OP-SFs lying perpendicular to the viewing direction (RP_0 region). (*b*) A HAADF-STEM cross-sectional view of another zone containing OP-SFs. These SFs coarsely delimit two regions: the $IG_{1/3}$ region (intergrowth, the subscript 1/3 refers to the local number of OP-SFs per RP half-period along the OP direction) where IP-SFs are missing, and the $RP_{1/3}$ region showing RP periodicity. In both panels (*a*) and (*b*), red lines/boxes indicate SFs. (*c*) A schematic diagram of a zone at the interface between an IG_α and an RP_α region, comprising $u = 1$ OP-SF for $v = 3$ RP half-periods ($\alpha = u/v$). The lateral mismatch between these two regions is accommodated over a coincidence supercell including $v(2N + 1)$ atomic planes, of vertical extent $H_\alpha^{SC} = vH_\alpha = vH_0 - 2u[d - (c/2)]$, by compression of the RP_α region near the IG_α/RP_α interface. In the compressed RP_α region, the RP half-period is shrunk to $H_\alpha = H_0 - 2\alpha[d - (c/2)]$.

Fig. 4(*a*) displays a HAADF-STEM cross-sectional view of a zone of the RP[5] sample (designated as the RP_0 region in the following) free of any OP-SFs lying parallel to the viewing direction and containing few OP-SFs lying perpendicular to the viewing direction. In this region, the RP half-period and the STO interplanar distance are, respectively, H_0 = 22.16 ± 0.015 Å and c = 3.921 ± 0.008 Å, as measured on the right-hand side of the HAADF-STEM image where no OP-SFs lying perpendicular to the viewing direction are detected (see Fig. S4 and its caption). This leads to d = 2.55 ± 0.04 Å, consistent with the (very sparse) values reported in the literature (Ohnishi *et al.*, 2008; Venkateswaran *et al.*, 1987; Saint-Girons *et al.*, 2016) and close to the SrO–SrO interplanar distance in bulk rocksalt SrO (2.58 Å). The average lattice parameter is $\overline{c}_0^{RP}$ = 4.029 ± 0.003 Å. H_0 is significantly larger than the RP half-periods reported in the literature, which typically range from 21.7 to 21.9 Å (Lee *et al.*, 2013*b*; Haeni *et al.*, 2001; Okude *et al.*, 2008; Elcombe *et al.*, 1991). As shown below, this discrepancy is due to the fact that the latter values are impacted by the presence of OP-SFs, while the value extracted from the local HAADF-STEM image of Fig. 4(*a*) corresponds to an OP-SF-free region.

The positions of reflections expected for the diffraction of RP_0-like regions, calculated from equation (1) using the H_0 value deduced from STEM, are indicated on the X-ray diffractogram of Fig. 3 (pale-blue bars). They match well with one of the shoulder sets attributed to the modulation of the RP period, and more precisely that corresponding to the largest RP period. This suggests that this series of reflections in the XRD pattern correspond to RP_0-like regions of the sample, free of OP-SFs. The other sets of shoulders correspond to the diffraction from sample regions in which the RP period is reduced with respect to the RP_0 regions. The set of shoulders for which this contraction is the largest (corresponding to the regions of the samples where the RP period is the smallest) are marked by grey bars in Fig. 3. The associated strain (deduced from the X-ray diffractogram) is −2.7%, much smaller than that expected for a local accommodation of strain due to OP-SFs (∼ −25%, see above). We show in the following that this results from a delocalization of the strain over supercells whose extension corresponds to several RP half-periods.

Fig. 4(*b*) shows a zone of the RP[5] sample containing OP-SFs. We define α as the ratio between the number of OP-SFs and the number of RP half-periods along the OP direction. For $\alpha = 0$, there are no OP-SFs (RP_0 region). Moreover, as each OP-SF goes through an integer number of RP half-periods (overwhelmingly one RP half-period, see Fig. 1 and its caption), α is a rational number. Finally, as the number of corner defects cannot exceed the number of IP-SFs (equal to the number of periods), and as each OP-SF generates two corner defects, α cannot exceed $\frac{1}{2}$. The value of α depends on the scale at which it is measured on the HAADF-STEM image. As shown below, the supercell marked by a white dotted square in Fig. 4(*b*) is a relevant scale to measure α for

the sample region shown in Fig. 4(*b*). It includes one OP-SF parallel to the viewing direction for three RP half-periods so that $\alpha = \frac{1}{3}$ at the scale of the supercell (SC). Its extension, denoted $H_{1/3}^{SC}$, where the subscript 1/3 refers to the local α value, corresponds to three RP half-periods, that is $3(2N_{OP} + 1)$ SrO or TiO_2 atomic planes.

Two regions can be defined in the supercell: the $IG_{1/3}$ region where IP-SFs are missing, and the $RP_{1/3}$ region where RP periodicity is maintained. The average lattice parameter in the $IG_{1/3}$ region is $\overline{c}_{1/3}^{IG} = 3.96 \pm 0.01$ Å, as measured on the HAADF-STEM image (Fig. S5). This is significantly smaller than that of the perfect RP_0 region ($\overline{c}_0^{RP} = 4.029 \pm 0.003$ Å). Indeed, the $IG_{1/3}$ lattice corresponds to an RP_0 lattice in which two IP-SFs are replaced by two STO half unit cells of smaller inter-reticular distance.

In the absence of any extrinsic strain mechanism affecting the structure in the $IG_{1/3}$ region, the average lattice parameter of the latter is expected to obey

$$\frac{\overline{c}_{1/3}^{IG}}{2} = \frac{1}{3(2N+1)}\left[3(2N+1)\frac{\overline{c}_0^{RP}}{2} - 2d + 2\frac{c}{2}\right],$$

which leads to $\overline{c}_{1/3}^{IG} = 3.957 \pm 0.006$ Å, using the values of $\overline{c}_0^{RP}$, d and c deduced from the HAADF-STEM image of Fig. 4(*a*). This is consistent with the value measured from Fig. 4(*b*), showing that the average lattice parameter in the $IG_{1/3}$ region is simply driven by the modification of the atomic layer stacking with respect to the undisturbed RP_0 region. The situation is different for the $RP_{1/3}$ region: the RP half-period in this region extracted from Fig. 4(*b*) (Fig. S5) is $H_{1/3} = 21.83 \pm 0.05$ Å, significantly smaller than that of the undisturbed RP_0 region ($H_0 = 22.16 \pm 0.015$ Å), while the atomic layer stacking is the same in both regions. The corresponding average lattice parameter is $\overline{c}_{1/3}^{RP} = 3.97 \pm 0.01$ Å.

The positions of reflections expected for the diffraction of $RP_{1/3}$-like regions, calculated from equation (1) using the $H_{1/3}$ value deduced from STEM, are indicated on the XRD diffractogram of Fig. 3. They match the experimental diffraction peaks, confirming that the latter result from a modulation of the RP period. Interestingly, the average lattice parameter in the $RP_{1/3}$ region equals that measured for the $IG_{1/3}$ region within experimental uncertainty: $\overline{c}_{1/3}^{IG} = \overline{c}_{1/3}^{RP}$. This suggests that a lateral strain transfer mechanism takes place between the $IG_{1/3}$ and $RP_{1/3}$ regions: the $RP_{1/3}$ region is laterally strained by the $IG_{1/3}$ region, so that both regions have the same average lattice parameter. This mechanism distributes the lateral mismatch between the $IG_{1/3}$ and $RP_{1/3}$ regions caused by the OP-SFs over the supercell (the latter is a coincidence supercell, comparable with those observed for some material systems in the domain epitaxy regime) (Narayan & Larson, 2003). The $RP_{1/3}$ region is laterally compressed by the $IG_{1/3}$ region so that both regions are in lateral registry over the coincidence supercell.

Fig. 4(*c*), schematizing the microstructure visible in Fig. 4(*b*), generalizes the strain transfer mechanism described above to a coincidence supercell of vertical extension H_α^{SC} corresponding to v RP half-periods including u OP-SFs. In such a configuration, the (rational) α value reads $\alpha = u/v$. The RP_α region is compressed by the IG_α region at the scale of the coincidence supercell, so that both regions have the same average lattice parameter, $\overline{c}_\alpha^{RP} = \overline{c}_\alpha^{IG}$. The coincidence supercell corresponds to v RP half-periods of an RP_0 structure in which $2u$ IP-SFs are replaced by $2u$ STO half unit cells, so that

$$H_\alpha^{SC} = vH_0 - 2u\left(d - \frac{c}{2}\right).$$

In addition, as the vertical extension of the coincidence supercell corresponds to $v(2N + 1)$ atomic planes, H_α^{SC} also reads $v(2N+1)(\overline{c}_\alpha^{RP}/2)$.This leads to

$$\overline{c}_\alpha^{RP} = \frac{2}{2N+1}\left[H_0 - 2\alpha\left(d - \frac{c}{2}\right)\right],$$

so that the RP half-period in the RP_α region reads

$$H_\alpha = \frac{2N+1}{2}\overline{c}_\alpha^{RP} = H_0 - 2\alpha\left(d - \frac{c}{2}\right). \qquad (2)$$

This equation gives the half-period of the RP structure when compressed by an IG_α region defined by a number of OP-SFs per RP half-period α. The larger α, the lower H_α, and as the maximum α value is $\frac{1}{2}$, the minimum half-period of the RP structure compressed by this mechanism is $H_{1/2} = 21.57 \pm 0.04$ Å (for an $RP_{1/2}$ region), calculated from equation (2) by substituting α by $\frac{1}{2}$ and H_0, d and c by their experimental values extracted from the analysis of the RP_0 HAADF-STEM image [Fig. 4(*a*)]. The positions of reflections expected for the diffraction of $RP_{1/2}$-like regions, calculated from equation (1), are indicated on the X-ray diffractogram of Fig. 3 (grey bars). They correspond to the set of shoulders associated with the lowest RP half-period (last shoulders on the high-$q_\perp$ side of the ± 1 RP satellite peaks), as expected for the largest possible value of α. This strong consistency between STEM observations and XRD measurements supports the assertion that the strain transfer mechanism described above results in local shrinkage of the RP period which depends on the local OP-SF concentration and leads to modulation of the XRD pattern. The fact that the strain generated by OP-SFs is entirely accommodated by deformation of the RP regions is compatible with the experimental observations reported by Stone *et al.* (2016). It is also consistent with the values of Young's modulus expected for the RP and IG regions. In fact, since Young's modulus of bulk SrO (~160 GPa; Johnston *et al.*, 1970) is significantly lower than that of bulk STO (~270 GPa; Samia & Salima, 2018; Carpenter, 2007), the SrO-rich RP regions are expected to be more prone to strain than the IG regions. The strain associated with this delocalized accommodation mechanism is

$$\varepsilon_\alpha = \frac{H_\alpha - H_0}{H_0} = -\frac{2\alpha}{H_0}\left(d - \frac{c}{2}\right).$$

Its maximum value is $\varepsilon_{1/2} = -2.8 \pm 0.2\%$ [calculated using the values of d, c and H_0 deduced from Fig. 4(*a*)], much lower than the $\sim -25\%$ expected for an accommodation localized around each corner defect, and of the same order of magnitude as that reported by Stone *et al.* (2016).

The lateral extent of the strain generated in the RP_α regions by the IG_α regions is denoted as L_{strain}. A tentative estimate of this extent is discussed below. In the schematic drawing shown in Fig. 4(*c*), the boundary between the RP_α and IG_α regions can be easily identified. However, the OP-SFs are *a priori* distributed randomly in the sample, and in particular they are not aligned vertically, which complicates the definition of the boundary between the IG_α and RP_α regions in the supercells comprising several OP-SFs ($u \geq 2$). For a set of OP-SFs to be collectively able to generate a strain in a common coincidence supercell according to the accommodation mechanism described above, these OP-SFs must be contained in a zone of the sample whose lateral extension is smaller than the lateral extension of the strain field L_{strain}. In other words, L_{strain} is the relevant lateral characteristic length to assess the distribution of α values within a sample.

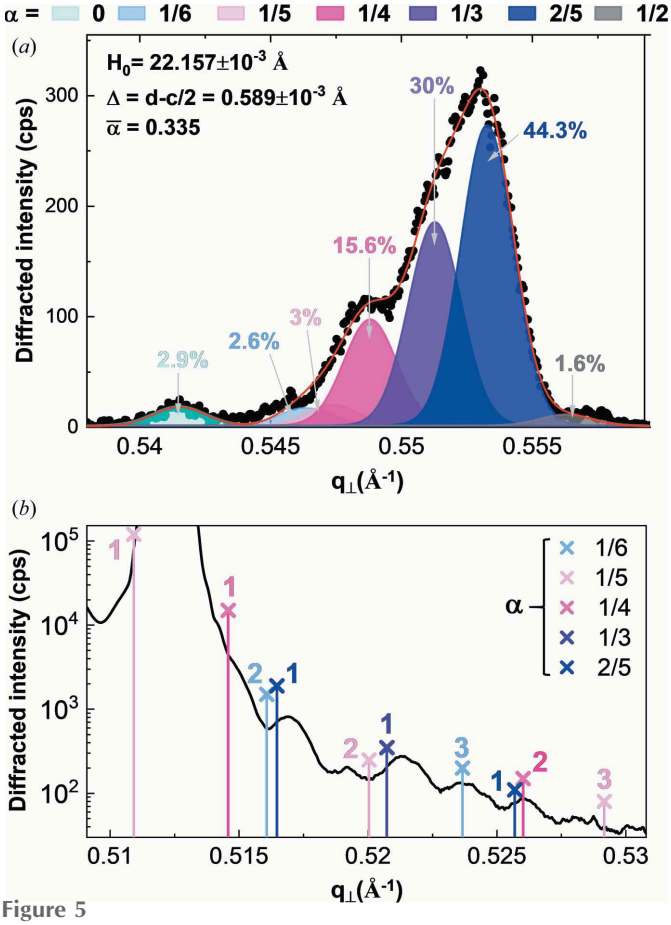

Figure 5
(*a*) An enlargement around the first-order RP satellite extracted from the X-ray diffractogram of Fig. 2, after background subtraction. The peak is fitted as a sum of Gaussian components corresponding to the diffraction of the different RP_α regions of the sample, with α ranging from 0 to $\frac{1}{2}$. The H_0 and $\Delta = [d - (c/2)]$ values are extracted from this fit, as well as the volume concentrations of the different RP_α regions. The average α value weighted by the areas of the Gaussian components is $\bar{\alpha} = 0.335$. (*b*) An enlargement of the large-$q_\perp$ tail of the zeroth-order peak of Fig. 2, in the region where supercell modulation peaks are detected. The crosses indicate the positions expected for these peaks, calculated from the H_0 and Δ values extracted from panel (*a*). The bar indices correspond to the satellite orders.

The results discussed above show that the residual mismatch related to the presence of OP-SFs is accommodated in a delocalized way, over coincidence supercells whose vertical extension H_α^{SC} corresponds to several RP half-periods, by local lateral compression of the RP lattice due to strain transfer from the adjacent IG region. This strain is spatially inhomogeneous as it depends on the local ratio between the number of OP-SFs and the number of RP half-periods, α. This is expected to broaden the X-ray diffraction peaks, as observed experimentally.

Even though they are consistent with the XRD measurements and the sparse data of the literature, the results based on STEM analyses presented above may somehow be biased because it can be difficult to detect all the OP-SFs lying perpendicular to the viewing direction. XRD measurements are expected to produce more reliable information, as such measurements intrinsically allow all the defects present in the sample to be taken into account on a macroscopic scale. We show in the following that analysing the XRD peak broadening produced by OP-SFs provides further information about the distribution of these defects in the sample. It is more convenient to proceed to this analysis on one of the RP satellite peaks rather than on the zeroth-order peak, as the very intense STO substrate reflection overlaps with the latter. Fig. 5(*a*) displays an enlargement of the RP X-ray diffractogram around the first-order RP satellite region. This curve is the sum of several components, each corresponding to the diffraction of all RP_α regions of the sample sharing the same α. The number of components corresponds to the number of different α values necessary to describe the OP-SF distribution in the sample, *i.e.* to the number of different coincidence supercell configurations. A relevant set of α values must first be chosen. α is rational (defined as u/v, where v is the supercell vertical extension in units of RP half-periods, and u the number of OP-SFs in the supercell) and obeys $0 \leq \alpha \leq \frac{1}{2}$. Denoting the largest supercell vertical extension in the sample as v_{max}, the set of possible α values is the set of u/v rational numbers satisfying $0 \leq \alpha \leq \frac{1}{2}$ and $v \leq v_{max}$. Choosing the set of α values is therefore simply choosing v_{max}. This set of α values is denoted as

$$\alpha_{set} = (\alpha_0 = 0, \ldots, \alpha_k, \ldots \alpha_{n-1}).$$

The half-period of the RP_{α_k} region associated with the kth value, α_k, is given by $H_{\alpha_k} = H_0 - 2\alpha_k\Delta$, with $\Delta = d - c/2$, and the centre of the associated component is given by

$$q_{\alpha_k} = \frac{L(2N_{OP}+1)}{2H_{\alpha_k}}\left[1 + \frac{2i}{L(2N+1)}\right],$$

with $L = 2$ and $i = 1$ (first-order RP satellite).

The kth component is described as a Gaussian of half-width at half-maximum w and of integral area A_k,

$$G(q_\perp, H_0, \Delta, w, A_k, \alpha_k) = \frac{A_k}{w}\left(\frac{\ln(2)}{\pi}\right)^{1/2}\exp\left[-\ln(2)\left(\frac{q_\perp - q_{\alpha_k}}{w}\right)^2\right],$$

H_0, Δ and w being shared between all components. Finally, the curve was fitted using the function

$$F(q_\perp, H_0, \Delta, w, A_{\rm set}, \alpha_{\rm set}) = \sum_{k=0}^{n-1} G(q_\perp, H_0, \Delta, w, A_k, \alpha_k),$$

with $A_{\rm set} = (A_0, \ldots, A_k, \ldots A_{n-1})$.

The shape of the curve in Fig. 5(*a*) allows us to estimate the number of components (n) at 6 or 7, which corresponds to two possible sets of α values, namely $\alpha_{\rm set\,1} = (0, \frac{1}{5}, \frac{2}{5}, \frac{1}{4}, \frac{1}{3}, \frac{1}{2})$ (all $u/v \leq \frac{1}{2}$ rational values so that $v \leq 5$) and $\alpha_{\rm set\,2} = (0, \frac{1}{6}, \frac{1}{5}, \frac{2}{5}, \frac{1}{4}, \frac{1}{3}, \frac{1}{2})$ (all $u/v \leq \frac{1}{2}$ rational values so that $v \leq 6$). Fitting the curve with $\alpha_{\rm set\,1}$ gives a poor result, in particular because the component centred at $q_{1/6}$ (corresponding to $\alpha = \frac{1}{6}$) is required for a correct description of the shoulder around $q_\perp = 0.545$ Å^{-1}. The best fit was obtained with $\alpha_{\rm set\,2} = (0, \frac{1}{6}, \frac{1}{5}, \frac{1}{4}, \frac{1}{3}, \frac{2}{5}, \frac{1}{2})$ by adjusting ten parameters, namely H_0, Δ and w (shared by all components) and the seven A_k integrated areas. The match between the fitted curve and the experimental data is particularly good ($\chi^2 = 0.995$). This shows that the vertical extension of the coincidence supercells ranges from two ($\alpha = \frac{1}{2}$) to six ($\alpha = \frac{1}{6}$) RP half-periods. For each supercell size, all configurations obeying $\alpha \leq \frac{1}{2}$ are detected. The fit leads to $H_0 = 22.157 \pm 0.001$ Å and $\Delta = d - (c/2) = 0.589 \pm 0.001$ Å. These values are consistent with those extracted from the TEM experiments and representative for the entire sample. They allow refining of the values of c and d: $c = 3.9214 \pm 0.0003$ Å and $d = 2.549 \pm 0.001$ Å. Note that c is slightly larger than the bulk STO lattice parameter (3.905 Å) by approximately 0.4%. Comparable expansion, although never reported experimentally to the best of our knowledge, has been predicted theoretically by several authors (Guan *et al.*, 2015; Fennie & Rabe, 2003) and attributed to significant rumpling of the extra SrO layers (Noguera, 2000; Benedek *et al.*, 2008). Such rumpling has been confirmed experimentally (Stone *et al.*, 2016; Venkateswaran *et al.*, 1987). The volume fractions of the RP_α regions, extracted from $A_{\rm set}$, are given in Fig. 5(*a*). They reflect the OP-SF distribution along the OP direction in the sample. The average value of α, weighted by the volume fractions of the RP_α regions, is $\overline{\alpha} = 0.335 \pm 0.001$.

We now discuss the series of reflections decorating the high-$q_\perp$ side of the zeroth-order peak, marked by red stars in Fig. 3 and highlighted in the enlargement displayed in Fig. 5(*b*). In the latter figure, the bars indicate the positions of the satellite peaks calculated for superlattices whose periods equal the size of the different coincidence supercells $H_\alpha^{\rm SC}$,

$$q_\alpha^{\rm SC}(i) = \frac{L}{\overline{c}_\alpha} + \frac{i}{H_\alpha^{\rm SC}} = \frac{1}{H_0 - 2\alpha\Delta}\left[\frac{(2N+1)L}{2} + \frac{i}{v}\right],$$

where

$$\overline{c}_\alpha = \overline{c}_\alpha^{\rm RP} = \overline{c}_\alpha^{\rm IG} = 2\frac{H_0 - 2\alpha\Delta}{(2N+1)L}$$

is the average lattice parameter over the supercell, $L = 2$ is the diffraction order, i is the satellite order [bar indices in Fig. 5(*b*)] and v is the vertical extension of the supercell in units of RP half-periods. The reflections corresponding to $\alpha = 0$ and $\alpha = \frac{1}{2}$ are superimposed on the satellite reflections of the RP_0 and $\mathrm{RP}_{1/2}$ regions and do not appear in Fig. 5(*b*). The calculated positions are close to the centres of the experimental peaks in Fig. 5(*b*), which tends to indicate that the latter result from a periodic structuration of the layer at the scale of the coincidence supercells. Hence, the strain transfer mechanism accommodating the mismatch caused by the OP-SFs generates a periodic strain in the thin layer, the period of which corresponds to the vertical extension of the coincidence supercells. The coherence and homogeneity of this mechanism are sufficient to give rise to satellite peaks of order up to 3 on the X-ray diffractogram. This reinforces the idea of a strong delocalization of the mismatch accommodation across the structure, which in turn affects the organization of the atomic stack along the growth axis over a characteristic length of several coincidence supercells.

One of the striking features of the OP-SF distribution deduced from Fig. 5(*a*) is the low fraction of RP_0 regions in the sample (2.9%). This observation allows us to estimate $L_{\rm strain}$ without direct measurement. $L_{\rm strain}$ is large enough for all RP regions to be strained by IG regions, which amounts to saying that $L_{\rm strain}$ is of the order of half the average distance between two OP-SFs along the IP direction. The latter was estimated to be 157 Å from the large-field HAADF-STEM view displayed in Fig. 1(*a*), so that $L_{\rm strain} \simeq 80$ Å, *i.e.* ∼20 ML. This value is of the same order as, but slightly larger than, that reported by Stone *et al.* (2016) for an RP[6]/IG[19] interface, namely 8–10 ML.

4. Conclusions

This work elucidates how the residual mismatch related to the presence of OP-SFs in STO-based RP thin layers is accommodated. We found that the mismatch is distributed over coincidence supercells of different sizes up to six RP half-periods and accommodated by local lateral compression of the RP lattice, which takes the average lattice parameter of the adjacent intergrowth region. This delocalized mechanism gives rise to a periodic strain of the structure with a coherence length of several coincidence supercells, *i.e.* several tens of nanometres. The resulting modulation of the RP period is detectable by XRD.

Analysis of the X-ray diffractograms allows the determination of the OP-SF distribution along the growth axis. It also allows us to measure separately and accurately the STO lattice parameter ($c = 3.9214 \pm 0.0003$ Å) and the SrO–SrO interreticular distance ($d = 2.549 \pm 0.001$ Å) in the RP lattice. It provides, for the first time to the best of our knowledge, a measure of the RP[5] half-period not distorted by OP-SFs, namely $H_0 = 22.157 \pm 0.001$ Å. All these parameters are accessible by simple non-destructive out-of-plane XRD measurements, representative of the layer at a macroscopic scale.

These results open an important prospect towards a better understanding of the incorporation of OP-SFs in RP thin layers and a more precise quantification of their spatial distribution. This is all the more important since OP-SFs are

the main or even the only defects accommodating stoichiometry imbalances in RP phases with a significant impact on their functional properties.

5. Related literature

For further literature related to the supporting information, see Smith *et al.* (2017).

Funding information

The following funding is acknowledged: Agence Nationale de la Recherche (CEAS-OFM project, grant No. ANR-21-CE24-0003).

References

Balachandran, P. V., Young, J., Lookman, T. & Rondinelli, J. M. (2017). *Nat. Commun.* **8**, 14282.

Barone, M. R., Dawley, N. M., Nair, H. P., Goodge, B. H., Holtz, M. E., Soukiassian, A., Fleck, E. E., Lee, K., Jia, Y., Heeg, T., Gatt, R., Nie, Y., Muller, D. A., Kourkoutis, L. F. & Schlom, D. G. (2021). *APL Mater.* **9**, 021118.

Barone, M. R., Jeong, M., Parker, N., Sun, J., Tenne, D. A., Lee, K. & Schlom, D. G. (2022). *APL Mater.* **10**, 091106.

Benedek, N. A., Elsässer, C. & Finnis, M. W. (2008). *J. Phys. Conf. Ser.* **94**, 012005.

Benedek, N. A., Rondinelli, J. M., Djani, H., Ghosez, P. & Lightfoot, P. (2015). *Dalton Trans.* **44**, 10543–10558.

Birch, J., Sundgren, J. E. & Fewster, P. F. (1995). *J. Appl. Phys.* **78**, 6562–6568.

Birol, T., Benedek, N. A. & Fennie, C. J. (2011). *Phys. Rev. Lett.* **107**, 257602.

Bowen, D. K. & Tanner, B. K. (1998). *High Resolution X-ray Diffractometry and Topography*. Boca Raton: CRC Press.

Carpenter, M. A. (2007). *Am. Mineral.* **92**, 309–327.

Castell, M. R. (2002). *Surf. Sci.* **505**, 1–13.

Dawley, N. M., Goodge, B. H., Egger, W., Barone, M. R., Kourkoutis, L. F., Keeble, D. J. & Schlom, D. G. (2020*a*). *Appl. Phys. Lett.* **117**, 062901.

Dawley, N. M., Marksz, E. J., Hagerstrom, A. M., Olsen, G. H., Holtz, M. E., Goian, V., Kadlec, C., Zhang, J., Lu, X., Drisko, J. A., Uecker, R., Ganschow, S., Long, C. J., Booth, J. C., Kamba, S., Fennie, C. J., Muller, D. A., Orloff, N. D. & Schlom, D. G. (2020*b*). *Nat. Mater.* **19**, 176–181.

Dawley, N. M., Pek, E. K., Lee, C. H., Ragasa, A. J., Xiong, X., Lee, K., Phillpot, S. R., Chernatynskiy, A. V., Cahill, D. G. & Schlom, D. G. (2021). *Appl. Phys. Lett.* **118**, 091904.

Elcombe, M. M., Kisi, E. H., Hawkins, K. D., White, T. J., Goodman, P. & Matheson, S. (1991). *Acta Cryst.* B**47**, 305–314.

Fennie, C. J. & Rabe, K. M. (2003). *Phys. Rev. B*, **68**, 184111.

Fleck, E. E., Barone, M. R., Nair, H. P., Schreiber, N. J., Dawley, N. M., Schlom, D. G., Goodge, B. H. & Kourkoutis, L. F. (2022). *Nano Lett.* **22**, 10095–10101.

Guan, L., Li, M., Li, X., Feng, L., Teng, F., Liu, B., Wei, Z. & Musgrave, C. B. (2015). *Comput. Mater. Sci.* **96**, 223–228.

Haeni, J. H., Theis, C. D., Schlom, D. G., Tian, W., Pan, X. Q., Chang, H., Takeuchi, I. & Xiang, X. (2001). *Appl. Phys. Lett.* **78**, 3292–3294.

Haislmaier, R. C., Stone, G., Alem, N. & Engel-Herbert, R. (2016). *Appl. Phys. Lett.* **109**, 043102.

Hawkins, K., White, T. J. & Smith, F. T. (1991). *Philos. Trans. R. Soc. London A*, **336**, 541–569.

Iwazaki, Y. T., Suzuki, S., Sekiguchi, S. & Fujimoto, M. (1999). *Jpn. J. Appl. Phys.* **38**, L1443.

Johnston, D. L., Thrasher, P. H. & Kearney, R. J. (1970). *J. Appl. Phys.* **41**, 427–428.

Jungbauer, M., Hühn, S., Egoavil, R., Tan, H., Verbeeck, J., Van Tendeloo, G. & Moshnyaga, V. (2014). *Appl. Phys. Lett.* **105**, 251603.

Kajdos, A. P. & Stemmer, S. (2014). *Appl. Phys. Lett.* **105**, 191901.

Kamba, S., Samoukhina, P., Kadlec, F., Pokorny, J., Petzelt, J., Reaney, I. M. & Wise, P. L. (2003). *J. Eur. Ceram. Soc.* **23**, 2639–2645.

Lee, C.-H., Orloff, N. D., Birol, T., Zhu, Y., Goian, V., Rocas, E., Haislmaier, R., Vlahos, E., Mundy, J. A., Kourkoutis, L. F., Nie, Y., Biegalski, M. D., Zhang, J., Bernhagen, M., Benedek, N. A., Kim, Y., Brock, J. D., Uecker, R., Xi, X. X., Gopalan, V., Nuzhnyy, D., Kamba, S., Muller, D. A., Takeuchi, I., Booth, J. C., Fennie, C. J. & Schlom, D. G. (2013*a*). *Nature*, **502**, 532–536.

Lee, C. H., Podraza, N. J., Zhu, Y., Berger, R. F., Shen, S., Sestak, M., Collins, R. W., Kourkoutis, L. F., Mundy, J. A., Wang, H., Mao, Q., Xi, X., Brillson, L. J., Neaton, J. B., Muller, D. A. & Schlom, D. G. (2013*b*). *Appl. Phys. Lett.* **102**, 122901.

Lee, J. H., Luo, G., Tung, I. C., Chang, S. H., Luo, Z., Malshe, M., Gadre, M., Bhattacharya, A., Nakhmanson, S. M., Eastman, J. A., Hong, H., Jellinek, J., Morgan, D., Fong, D. D. & Freeland, J. W. (2014). *Nat. Mater.* **13**, 879–883.

Lee, K. H., Kim, S. W., Ohta, H. & Koumoto, K. (2006). *J. Appl. Phys.* **100**, 063717.

Liu, S., Avdeev, M., Liu, Y., Johnson, M. R. & Ling, C. D. (2016). *Inorg. Chem.* **55**, 1403–1411.

McCarthy, G. J., White, W. B. & Roy, R. (1969). *J. Am. Ceram. Soc.* **52**, 463–467.

McCoy, M. A., Grimes, R. W. & Lee, W. E. (1997). *Philos. Mag. A*, **75**, 833–846.

Moritomo, Y., Asamitsu, A., Kuwahara, H. & Tokura, Y. (1996). *Nature*, **380**, 141–144.

Narayan, J. & Larson, B. C. (2003). *J. Appl. Phys.* **93**, 278–285.

Nie, Y. F., Zhu, Y., Lee, C.-H., Kourkoutis, L. F., Mundy, J. A., Junquera, J., Ghosez, P., Baek, D. J., Sung, S., Xi, X. X., Shen, K. M., Muller, D. A. & Schlom, D. G. (2014). *Nat. Commun.* **5**, 4530.

Noguera, C. (2000). *Philos. Mag. Lett.* **80**, 173–180.

Oh, Y. S., Luo, X., Huang, F.-T., Wang, Y. & Cheong, S. W. (2015). *Nat. Mater.* **14**, 407–413.

Ohnishi, T., Shibuya, K., Yamamoto, T. & Lippmaa, M. (2008). *J. Appl. Phys.* **103**, 103703.

Okude, M. A., Ohtomo, T., Kita, T. & Kawasaki, M. (2008). *Appl. Phys. Expr.* **1**, 081201.

Orloff, N. D., Tian, W., Fennie, C. J., Lee, C.-H., Gu, D., Mateu, J., Xi, X. X., Rabe, K. M., Schlom, D. G., Takeuchi, I. & Booth, J. C. (2009). *Appl. Phys. Lett.* **94**, 042908.

Pitcher, M. J., Mandal, P., Dyer, M. S., Alaria, J., Borisov, P., Niu, H., Claridge, J. B. & Rosseinsky, M. J. (2015). *Science*, **347**, 420–424.

Razaghi Pey Ghaleh, M. M., d'Esperonnat, C., Botella, S., Cueff, R., Bachelet, R. & Saint-Girons, G. (2021). *CrystEngComm*, **23**, 2269–2275.

Ruddlesden, S. N. & Popper, P. (1957). *Acta Cryst.* **10**, 538–539.

Ruddlesden, S. N. & Popper, P. (1958). *Acta Cryst.* **11**, 54–55.

Saint-Girons, G., Bachelet, R., Moalla, R., Meunier, B., Louahadj, L., Canut, B., Carretero-Genevrier, A., Gazquez, J., Regreny, P., Botella, C., Penuelas, J., Silly, M. G., Sirotti, F. & Grenet, G. (2016). *Chem. Mater.* **28**, 5347–5355.

Samia, B. & Salima, S. (2018). *Model. Meas. Control B*, **87**, 230–235.

Seshadri, R., Hervieu, M., Martin, C., Maignan, A., Domenges, B., Raveau, B. & Fitch, A. N. (1997). *Chem. Mater.* **9**, 1778–1787.

Shibuya, K., Mi, S., Jia, C. L., Meuffels, P. & Dittmann, R. (2008). *Appl. Phys. Lett.* **92**, 241918.

Sloan, J., Battle, P. D., Green, M. A., Rosseinsky, M. J. & Vente, J. F. (1998). *J. Solid State Chem.* **138**, 135–140.

Smith, E. H., King, P. D. C., Soukiassian, A., Ast, D. G. & Schlom, D. G. (2017). *Appl. Phys. Lett.* **111**, 131903.

Stone, G., Ophus, C., Birol, T., Ciston, J., Lee, C. H., Wang, K., Fennie, C. J., Schlom, D. G., Alem, N. & Gopalan, V. (2016). *Nat. Commun.* **7**, 12572.

Tian, W., Haeni, J. H., Schlom, D. G., Hutchinson, E., Sheu, B. L., Rosario, M. M., Schiffer, P., Liu, Y., Zurbuchen, M. A. & Pan, X. Q. (2007). *Appl. Phys. Lett.* **90**, 022507.

Tian, W., Pan, X. Q., Haeni, J. H. & Schlom, D. G. (2001). *J. Mater. Res.* **16**, 2013–2026.

Tilley, R. J. D. (1977). *J. Solid State Chem.* **21**, 293–301.

Tokuda, Y., Kobayashi, S., Ohnishi, T., Mizoguchi, T., Shibata, N., Ikuhara, Y. & Yamamoto, T. (2011). *Appl. Phys. Lett.* **99**, 173109.

Udayakumar, K. R. & Cormack, A. N. (1998). *J. Am. Ceram. Soc.* **71**, C469–C471.

Venkateswaran, U., Strössner, K., Syassen, K., Burns, G. & Shafer, M. W. (1987). *Solid State Commun.* **64**, 1273–1277.

Williams, T., Lichtenberg, F., Reller, A. & Bednorz, G. (1991). *Mater. Res. Bull.* **26**, 763–770.

Wise, P. L., Reaney, I. M., Lee, W. E., Price, T. J., Iddles, D. M. & Cannell, D. S. (2001). *J. Eur. Ceram. Soc.* **21**, 2629–2632.

Yang, C., Wang, Y., Putzky, D., Sigle, W., Wang, H., Ortiz, R. A., Logvenov, G., Benckiser, E., Keimer, B. & van Aken, P. A. (2022). *Symmetry*, **14**, 464.

Zhu, Y., Lee, D., Schlom, D. & Muller, D. (2011). *Microsc. Microanal.* **17**, 1396–1397.